

Supplementary Materials for  
**Quasi–two-dimensional ferroelectricity with multiple switchable polarization states in N-H coinjected perovskite manganites**

Xian-Kui Wei *et al.*

Corresponding author: Xian-Kui Wei, [xkwei@xmu.edu.cn](mailto:xkwei@xmu.edu.cn); Lei Cao, [caoleiinhit@gmail.com](mailto:caoleiinhit@gmail.com)

*Sci. Adv.* **11**, eadx3747 (2025)  
DOI: 10.1126/sciadv.adx3747

**This PDF file includes:**

Figs. S1 to S12

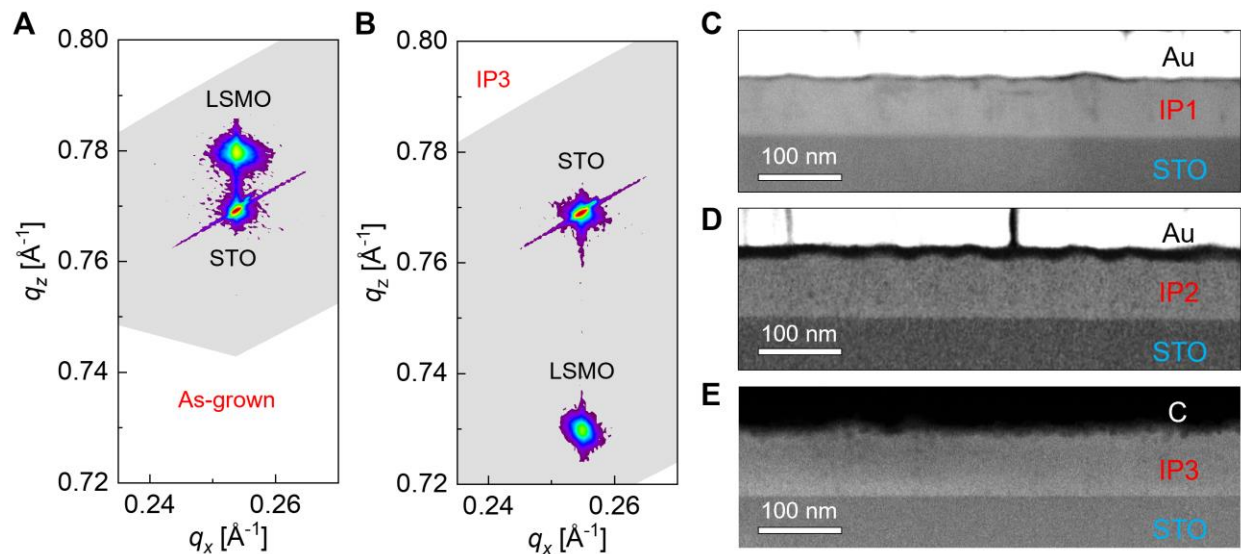


**Fig. S1. Structural characterization of NH-LSMO samples.** (A,B) Reciprocal space mapping of the as-grown and IP3 LSMO samples grown on STO substrates, respectively. (C-E) Cross-sectional HAADF STEM image of NH<sub>3</sub> plasma-treated IP1, IP2 and IP3 sample, respectively.

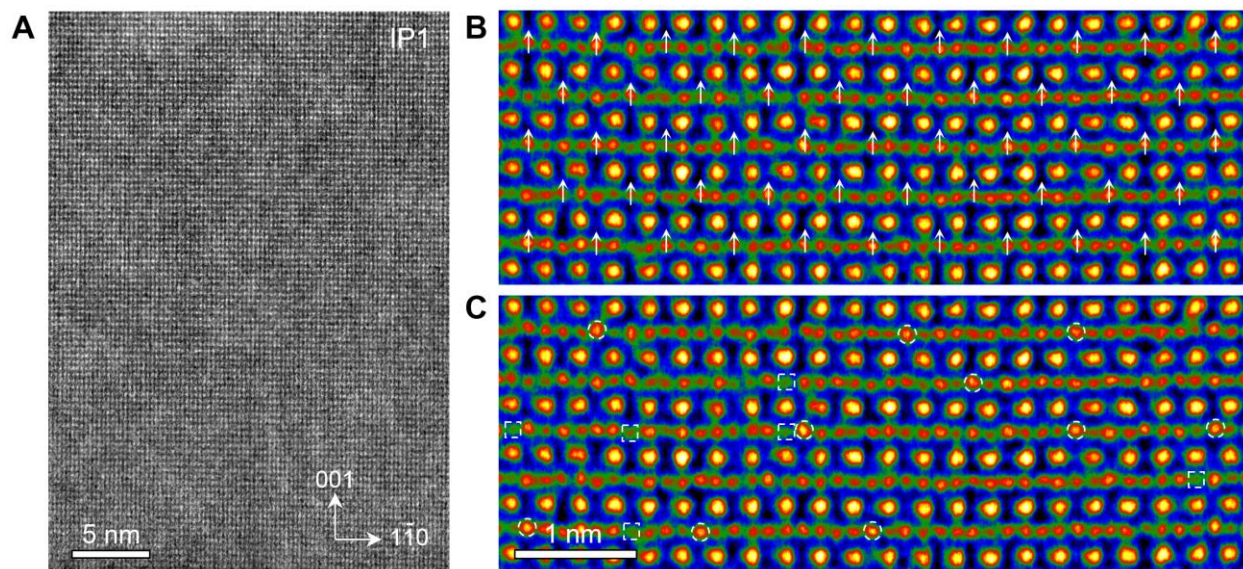


**Fig. S2. FD structure in the IP1 sample.** (A) HAADF-STEM image of IP1 sample viewed along  $[110]_p$  direction. (B) False-color iDPC image with highlight of oxygen displacements with large amplitude along  $z$  direction. (C) The same iDPC image with highlight of probable vacancies at O and Mn sites (squares) and anti-occupancy of cations at the O site (circles), given the potential contrast reversal, tunable by the imaging parameter of defocus, in the phase-contrast iDPC image.

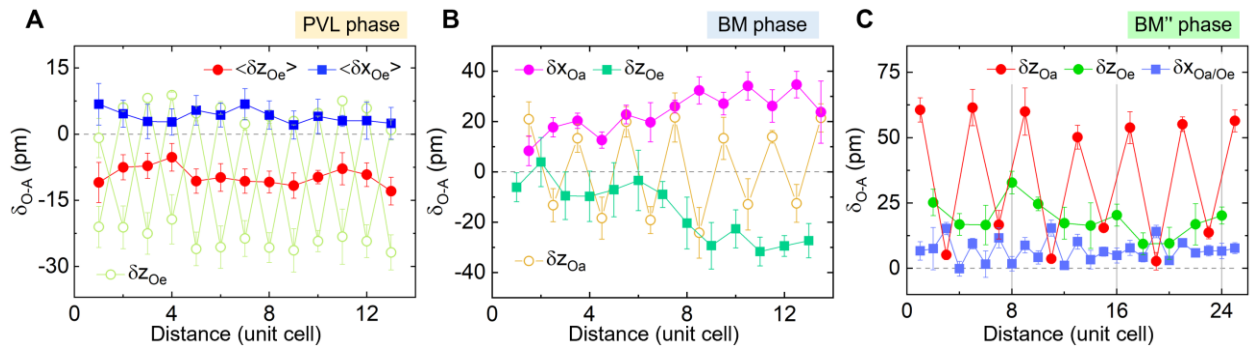


**Fig. S3. Relative oxygen displacements against centers of the A-site cations.** (A-C) Apical (Oa) and equatorial (Oe) oxygen shift profiles measured from (D) for the PVL phase, (H) for the BM phase, and (K) for the BM'' phase shown in Fig. 2.

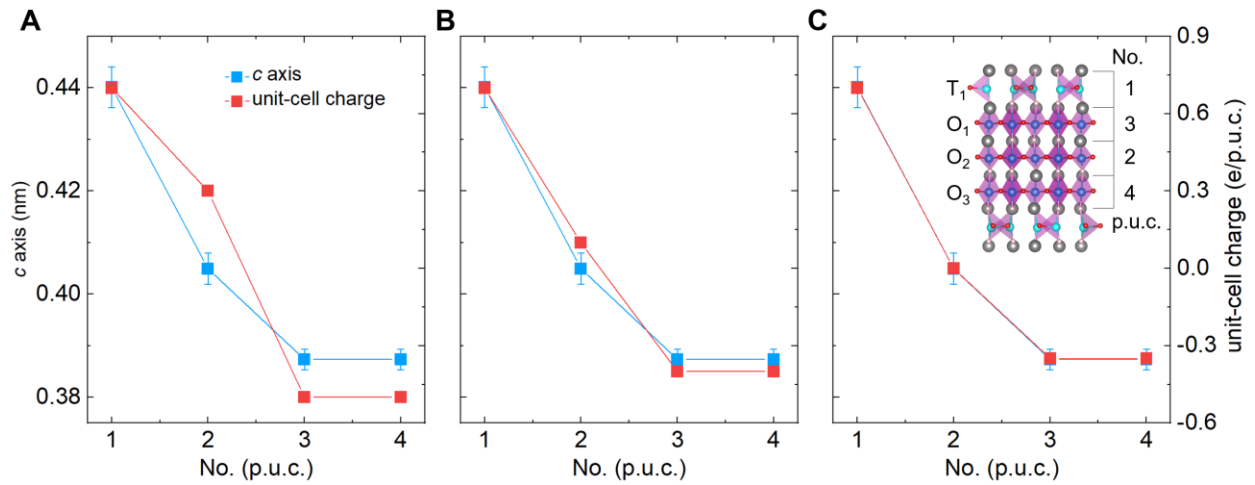


**Fig. S4. Linear scaling of unit-cell charge with *c* axis in the BM'' phase.** (A-C) The linear scaling relationship between *c* axis and charges per pseudocubic unit cell (p.u.c.) with consideration of Mn valence states at tetrahedral and octahedral sites from Mn<sub>T1</sub>, Mn<sub>O1</sub>, Mn<sub>O2</sub> to Mn<sub>O3</sub> as (A) 2+, 2.8+, 3.6+ to 2.8+, (B) 2+, 2.9+, 3.4+ to 2.9+, (C) 2+, 2.95+, 3.3+ to 2.95+. The inset in (C) illustrate the pseudocubic unit cell and the polyhedral units.

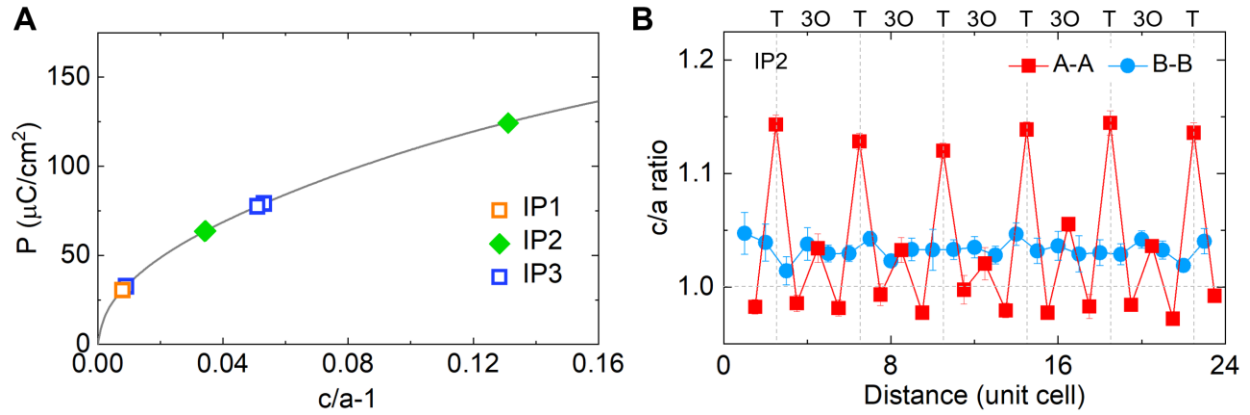


**Fig. S5. Polarization evaluation based on  $P^2 = \kappa(c/a - 1)$  relation in ordinary ferroelectrics.**

(A) The estimated polarization for IP1, IP2 and IP3 samples with the  $c_p/a_p$  ratio values measured from X-ray diffraction and atomic-resolution STEM measurement. (B) The lattice tetragonality ( $c/a$ ) ratio of adjacent pseudocubic unit cells in the BM'' phase. Although the polarization in unit cells with small  $c/a$  ratio ( $< 1.0$ ), measured from A-A columns, cannot be evaluated, the  $c/a$  ratio measured from B-B columns delivers a constant value, which corresponds to  $\langle P_z \rangle = 63.7 \mu\text{C}/\text{cm}^2$ . The coefficient  $\kappa$  is determined by using  $\text{PbTiO}_3$  with  $c/a = 1.064$  and  $P = 82 \mu\text{C}/\text{cm}^2$ .

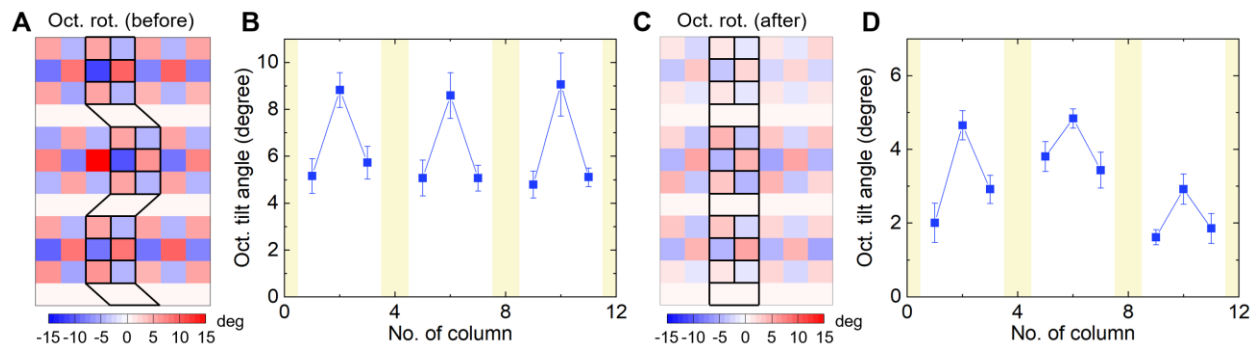


**Fig. S6. Electron-beam irradiation induced collective octahedral rotation in the BM'' phase.** (A,C) Anti-phase and in-phase octahedral rotation map of the BM'' phase before and after the electron-beam irradiation, respectively. (B,D) Plot of the octahedral rotation angle before and after the electron-beam irradiation, respectively.

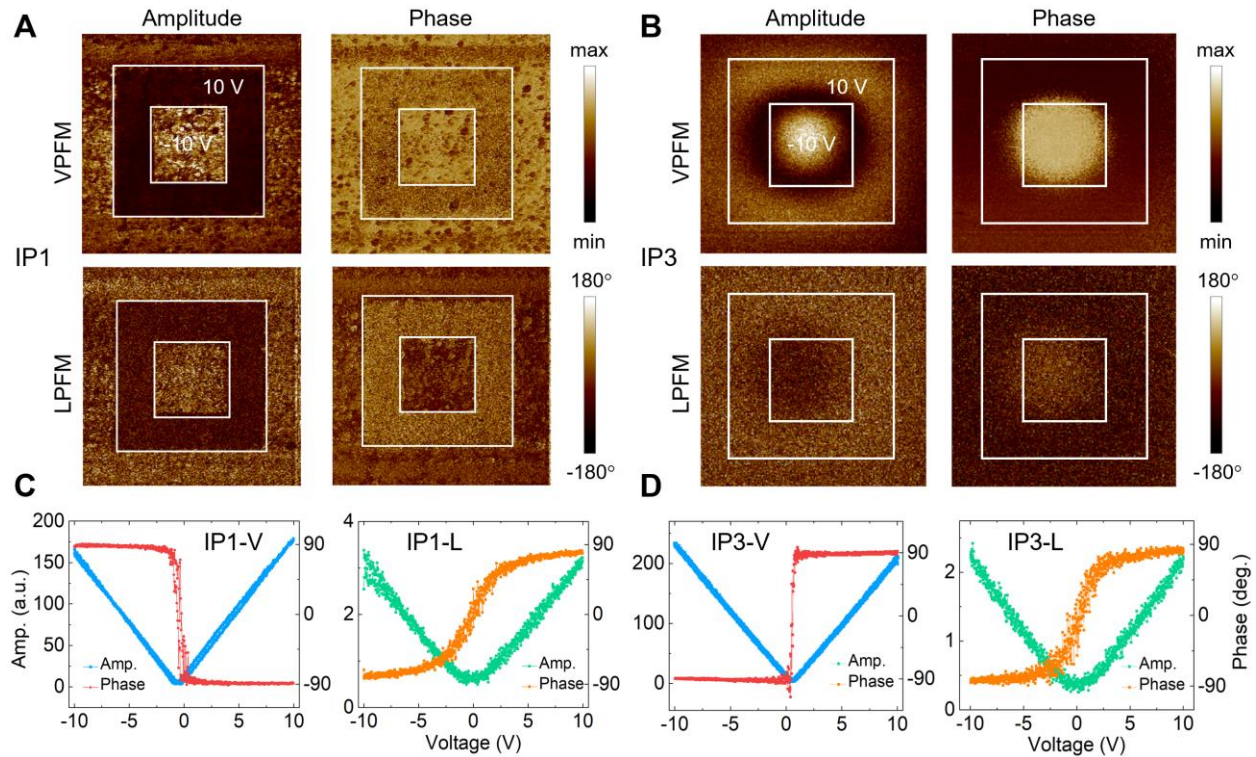


**Fig. S7. Volatile piezo-response in the FD phase of NH-LSMO with  $\delta \approx 0.125$  and 0.5.** (A,B) Vertical (V) and lateral (L) PFM amplitude and phase maps of IP1 and IP3 samples with the marked regions poled at  $\pm 10$  V with a test frequency of  $f = 0.1$  Hz and 0.2 Hz, respectively. (C,D) Typical V and L amplitude and phase hysteresis loops of the IP1 and IP3 samples, respectively. The size of each image is  $15 \times 15 \mu\text{m}^2$ .

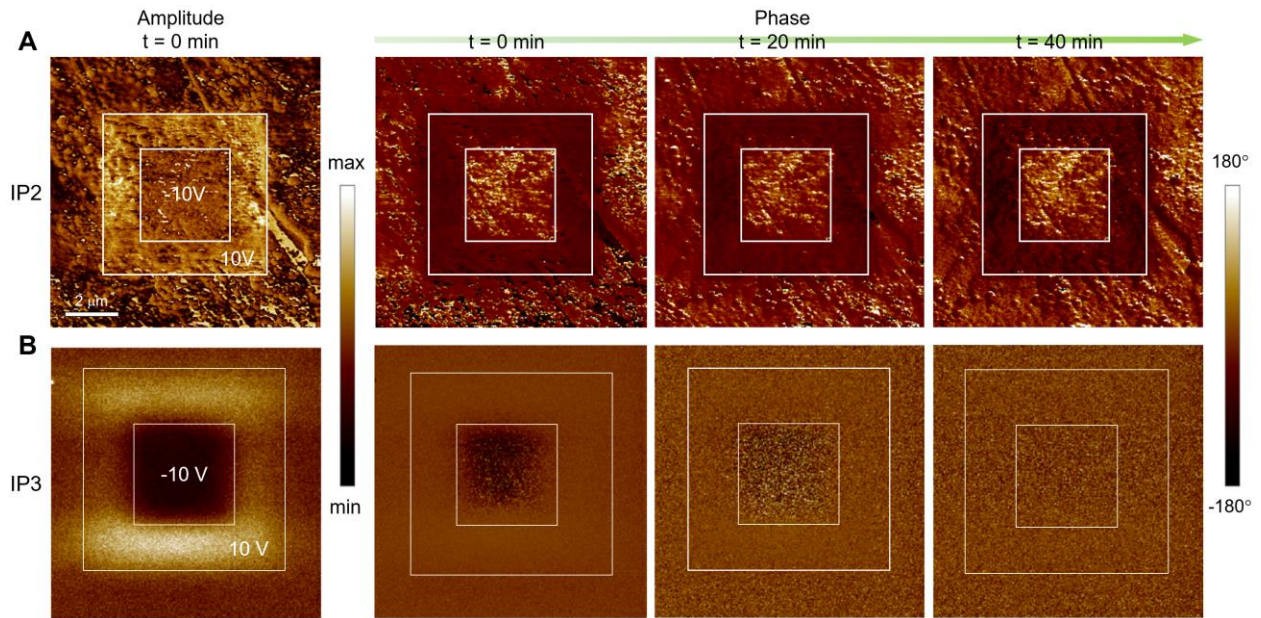


**Fig. S8. Time dependent polarization retention in IP2 and IP3 samples.** The square regions are vertically poled and switched by an applied PFM tip voltage of  $\pm 10$  V at  $t = 0$  min and then re-scanned at  $t = 20$  and  $40$  min, respectively.

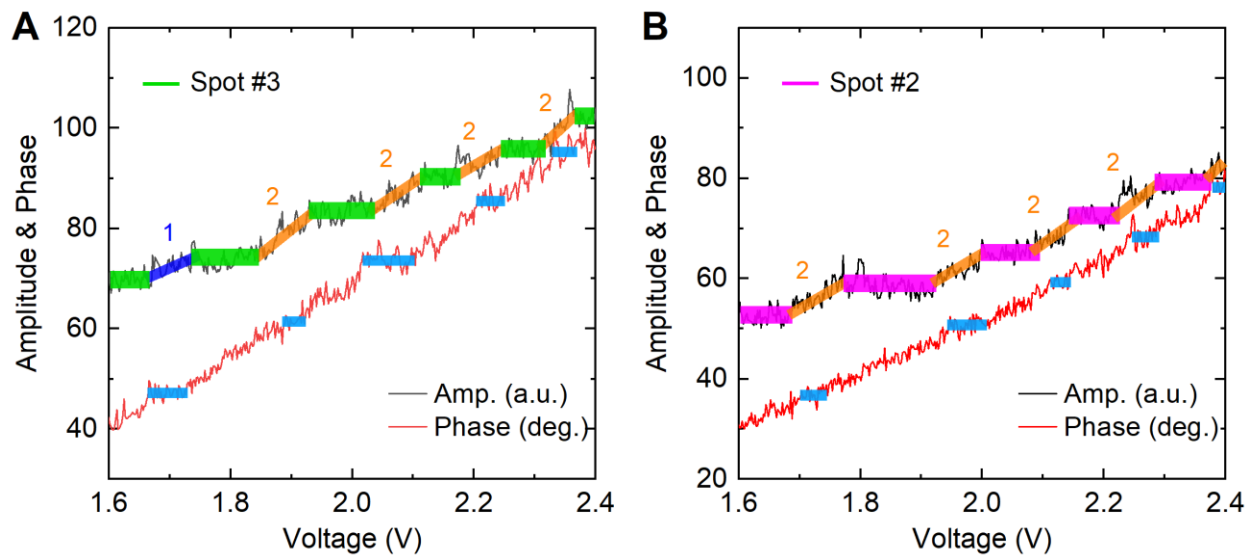


**Fig. S9. Electric field-induced step-type PFM response.** **A,B**, Voltage dependent amplitude and phase profiles for Spot #3 and #2 measured under application of a *dc* electric field, respectively.

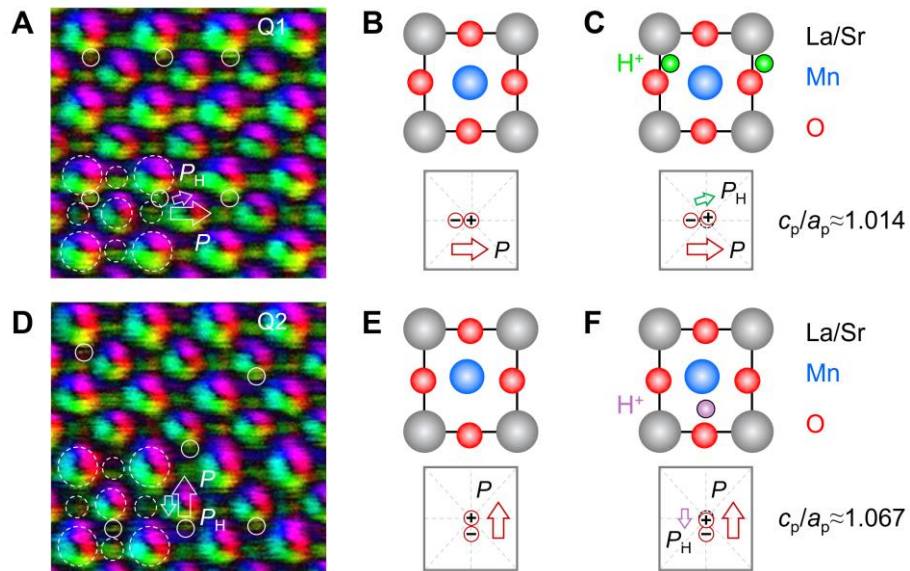


**Fig. S10. H intercalation induced change in unit-cell polarization.** (A,D) Magnified Q1 and Q2 regions with H atoms (solid circles) near the A-site (upper) and B-site (lower) columns, respectively. (B,C,E,F) The relative atom shifts without (B,E) and with (C,F) consideration of intercalated hydrogen in the form of protons. The H induced electric dipole is marked by  $P_H$  with respect to the H-free unit-cell dipole  $P$ .

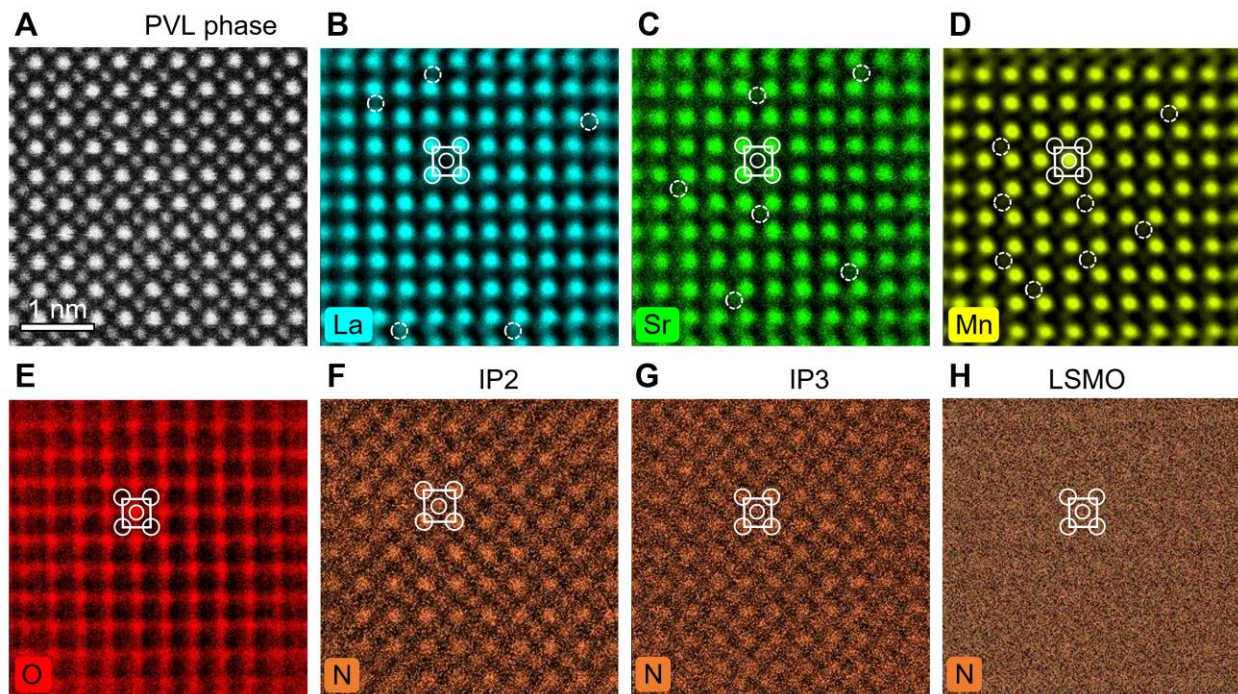


**Fig. S11. Atomic-resolution EDS maps.** (A-E) Representative elemental maps of La, Sr, Mn, O for the PVL phase, respectively. The white dashed circles mark the antisite defects such as  $\text{La}_\text{O}$ ,  $\text{Sr}_\text{Mn}$ ,  $\text{Sr}_\text{O}$  and  $\text{Mn}_\text{A}$ . (F-H) The EDS N maps for the IP2, IP3 samples and pure LSMO sample, respectively. The solid-line square denotes an La/Sr atom-based pseudocubic unit cell. One should note that during the long-time electron irradiation and data acquisition ( $\sim 45$  min for each set of data), the BM and BM'' phases have transformed to the PVL phase already.

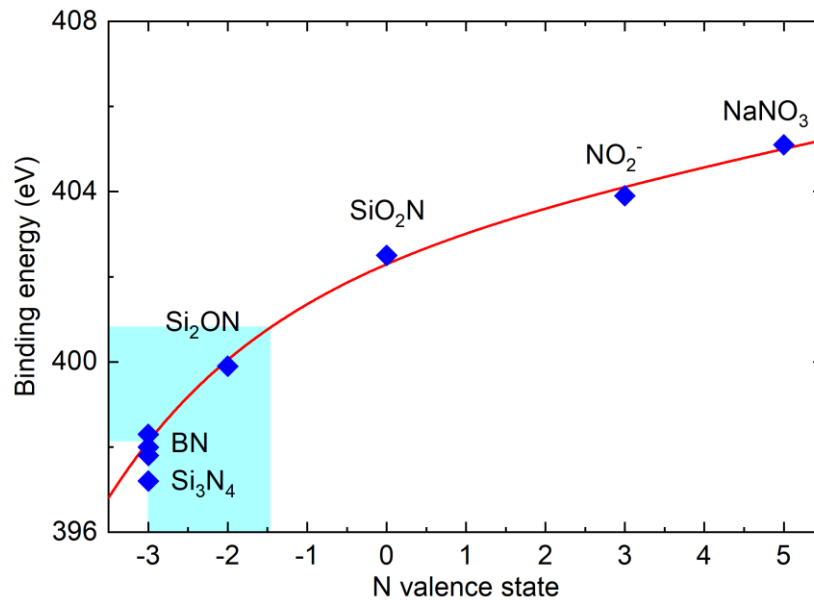


**Fig. S12. Relationship of binding energy with N valence state in inorganic compounds.** The names of specific compounds are labelled aside. The N valence state in the NH-LSMO samples are determined by referring to the fitted nonlinear profile (red solid line).